Fundamental Studies of $P(GeH_3)_3$, $As(GeH_3)_3$, and $Sb(GeH_3)_3$: Practical *n*-Dopants for New Group IV Semiconductors

A. V. G. Chizmeshya,[†] C. Ritter,[†] J. Tolle,[†] C. Cook,[‡] J. Menéndez,[‡] and J. Kouvetakis*[,†]

Department of Chemistry and Biochemistry and Department of Physics and Astronomy, Arizona State University, Tempe, Arizona 85287

Received July 20, 2006. Revised Manuscript Received September 25, 2006

We introduce a new chemical approach to the incorporation of high concentrations of active *n*-dopant atoms into group-IV semiconductors via low temperature, low cost, high efficiency routes involving carbon-free single-source inorganic hydrides. Controlled substitution of As into Ge-based semiconductors is made possible by the use of $As(GeH_3)_3$, which furnishes structurally and chemically compatible $AsGe_3$ molecular cores. $As(GeH_3)_3$ is synthesized in high purity yields (~75%) via a new single-step method based on reactions of GeH_3Br and $As[Si(CH_3)_3]_3$, circumventing the need for toxic and unstable starting materials as used in earlier approaches. We demonstrate the development of a viable route to the entire family of compounds $M(GeH_3)_3$ {M = P, As, Sb}, suitable for doping or superdoping applications of a wide range of functional materials. The structural, vibrational, and thermochemical properties of $M(GeH_3)_3$ are simulated for the first time via density functional theory calculations using both all-electron and effective core potentials. The vibrational calculations are in excellent agreement with the observed infrared spectra and the thermochemical stability is predicted to decrease with increasing molecular mass, in accord with experimental observations. The simulated structures show that the Ge−M−Ge angles decrease with increasing M size and further resolve inconsistencies with earlier gas electron diffraction measurements of $P(GeH_3)_3$. Bulk supercell calculations are then used to study the formation free energy of P, As, and Sb incorporation in bulk Ge, as well as the bond and lattice strains induced by the dopant atoms in the host diamond-structure lattice. As a first example of the usability of the $M(GeH_3)_3$ family, we demonstrate the successful doping of metastable $Ge_{1-y}Sn_y$ alloys. This represents a crucial step toward the goal of developing photonic devices, such as photodetectors and photovoltaic cells, based on $Ge_{1-y}Sn_y$. Infrared ellipsometry experiments demonstrate high carrier concentrations and excellent resistivities in $As(GeH_3)_3$-doped $Ge_{1-y}Sn_y$. The latter are only moderately higher than those measured in pure Ge for the same dopant levels.

Introduction

The standard approach for in situ *n*-type doping of group-IV semiconductors utilizes low order hydrides such as PH_3, AsH_3, and SbH_3. Unfortunately, the use of these gases for the fabrication of complex heterostructures is hampered by surface "poisoning" that affects growth rates and strong segregation effects that distort the targeted doping profiles. In addition, they are of limited use at the very low-temperature conditions required to grow metastable Sn-containing alloy semiconductors. They also pose safety concerns, because AsH_3 and PH_3 are highly toxic and can be lethal in relatively small doses. Solid sources of the elements can be used, but there are limits as to how much dopant concentration can be incorporated into the structure. Ion implantation techniques are controllable and reliable when the doping is needed to be near the film surface. For thick films it becomes difficult to obtain precise and homogeneous dopant distributions, since the ions gradually lose their energy as they travel through the film. Implantation can also cause significant structural damage to the target solids particularly Si−Ge−Sn optical semiconductors containing "soft" Ge−Sn and Si−Sn bonds. High temperature annealing steps to activate the dopants often lead to additional problems such as precipitation, strain relaxation, and phase segregation.

In this paper, we report the development of a new doping strategy based on $M(GeH_3)_3$ {M = P, As, Sb} hydrides that contain molecular cores composed of host and dopant atoms in a structural configuration compatible with *n*-type doping of the host. These carbon-free inorganic hydrides are co-deposited with appropriate concentrations of C/Si/Ge/Sn hydrides to form group IV semiconductor layers doped with the desired carrier type. The precursors are volatile but relatively stable at room temperature and react readily via elimination of benign H_2 byproducts. Their basic structural unit is comprised of a single P, As, or Sb center surrounded by three Ge atoms. As demonstrated in this work the incorporation of this geometry intact into the diamond structures of group IV materials produces a homogeneous substitution of the dopants at the lattice sites without clustering or segregation. The massive molecular units should lead to low diffusion and thus highly uniform compositional and strain profiles at the atomic level. This is in contrast to the *uncontrolled* (diffusion-driven) elemental mixing associated with conventional chemical vapor deposition (CVD) and implantation processes involving low order hydrides.

* To whom correspondence should be addressed. E-mail: jkouvetakis@asu.edu.
[†] Department of Chemistry and Biochemistry.
[‡] Department of Physics and Astronomy.

10.1021/cm061696j CCC: $33.50
Published on Web 11/18/2006

$M(GeH_3)_3$ hydrides with direct Ge−P, Ge−As, or Ge−Sb bonds in atomic arrangements that are structurally compatible with the covalent diamond lattice framework are expected to favor high free carrier concentrations under metastable growth conditions. For our initial proof-of-concept demonstration we focus on the doping of $Ge_{1-y}Sn_y$ alloys, but we expect the $As(GeH_3)_3$, $Sb(GeH_3)_3$, and $P(GeH_3)_3$ hydrides to be useful for doping or superdoping of elemental Ge, $Si_{1-x}Ge_x$, $Si_{1-x-y}Ge_xC_y$, and $Si_{1-x-y}Ge_xSn_y$. The objective of superdoping is to increase the density of states and induce covalent metallic and semimetallic character. Metallic, covalent materials are rare and have potential as metal−semiconductor contacts. Groundbreaking superconducting properties might also be achievable. Furthermore, the incorporation of large concentrations of group V species under metastable conditions could induce exotic polymorphic phases with novel elastic and electronic properties.

Several previous reports provide only some preliminary results of the synthesis of $P(GeH_3)_3$, $As(GeH_3)_3$, and $Sb(GeH_3)_3$ compounds and a very limited discussion of their fundamental physical properties.[1,2] Our objective in this study is to develop new and practical methods to prepare, isolate, purify, and handle these molecules in sufficient quantities to make them useful as chemical reagents as well as CVD gas sources. Key properties such as vapor pressure, thermal stability, and chemical reactivity are investigated by theory and experiment. Extensive *ab initio* studies are undertaken, for the first time, to elucidate the thermochemical properties and structural trends (bond lengths and angles) as related to their use as building blocks in the formation of tetrahedral semiconductors.

As a first application of our general method, we demonstrate the applicability of $As(GeH_3)_3$ as a CVD source for low temperature and high efficiency doping of $Ge_{1-y}Sn_y$ alloys. We have recently demonstrated device quality growth of a new class of optoelectronic semiconductors based on these alloys for $y < 0.2$. $Ge_{1-y}Sn_y$ undergoes a transition from an indirect to a direct gap for $y \sim 0.1$,[3] leading to the first direct-gap material fully integrated with Si technology. They cover a wide range of operating wavelengths in the IR and have been proposed as new active layers for a range of novel device structures such as strain engineered heterodiodes, multi-quantum well lasers, photodetectors, emitters, and modulators grown on Si (Soref, R.A.; et al. U.S. Patent 6,897,471, 2005). A remaining challenge, particularly from the point of view of device fabrication, is the development of *n*-doping strategies to incorporate desired levels of activated P, As, and Sb atoms without degrading the quality of the parent lattice. It should be noted that alloys based on Sn are inherently metastable and require low-temperature growth routes. Accordingly, traditional precursors based on As hydrides or metalorganics cannot be used to achieve the desired optical and electronic structure. By contrast, we demonstrate here that $As(GeH_3)_3$ is ideally suited for the doping of $Ge_{1-y}Sn_y$ alloys.

Synthetic Methods

The synthesis, properties and reactions of the $(Me_3Si)_3E$ and $(Me_3Ge)_3E$ (E = P, As, or Sb) compounds have been extensively described in the organometallic chemistry arena.[4−8] The corresponding C−H free analogs $(SiH_3)_3E$[9] and $(GeH_3)_3E$[1,2] have remained relatively unexplored despite of their potential relevance in semiconductor materials science as discussed above. The previously reported synthesis of $(GeH_3)_3E$[1,2] is obtained by the following reaction of GeH_3Br with $(SiH_3)_3E$:

$$3GeH_3Br + (SiH_3)_3E \rightarrow 3SiH_3Br + (GeH_3)_3E \quad (1)$$

No yield was reported for $(GeH_3)_3P$, and this product was described as a colorless liquid with a melting point of −83.8 °C and a vapor pressure of 1 Torr at 0 °C. The $(GeH_3)_3As$ and $(GeH_3)_3Sb$ analogs were prepared in very low yields (in certain cases only traces of the products were obtained) and were found to decompose slowly, over time, at room temperature. Although their vapor pressures were not reported, there was mention of distilling the liquids onto CsBr plates to obtain IR spectra. This indicates that they are sufficiently volatile to allow significant mass transport under vacuum. In an attempt to generate higher yields of these compounds, the $(GeH_3)_3P$ species was also produced by a redistribution reaction involving silylphosphines and germylphosphines in the presence of B_5H_9. In these reactions, B_5H_9 and GeH_3PH_2 were reacted in the gas phase at room temperature to produce $(GeH_3)_3P$ in 20% yield along with PH_3 and GeH_4 as described in ref 9. It should be noted that the silylphosphine starting materials utilized in the above syntheses are not practical as reagents for routine laboratory synthesis because they are difficult to produce in sufficient yields. Furthermore, the original syntheses of $(GeH_3)_3E$ are cumbersome and involve steps that can be potentially dangerous, especially for reagent level quantities.

To circumvent these problems we have developed a new and straightforward method to prepare the $(GeH_3)_3E$ family of compounds in high yield (∼70−75%). Our approach utilizes the common and relatively inexpensive organometallic derivatives $[(CH_3)_3Si)]_3E$ for which simple, large scale syntheses are well-established. The principal benefit is that large yields can be obtained via the single step synthetic reaction given by eq 2

$$3GeH_3Br + [(CH_3)_3Si]_3E \rightarrow 3(CH_3)_3Si\,Br + (GeH_3)_3E \quad (2)$$

This allows detailed characterization and purification at levels required for modern semiconductor materials applications,

(1) Cradock, S.; Ebsworth, E. A. V.; Davidson, G.; Woodard, L. A. *Chem. Commun.* **1965**, *21*, 515. Cradock, S.; Ebsworth, E. A. V. *J. Chem. Soc. A* **1967**, *8*, 1226. Wingeleth, D. E.; Norman, A. D. *Phosphorus Sulfur Relat. Elem.* **1988**, *39*, 123.
(2) Ebsworth, E. A. V.; Rankin, D. W. H.; Sheldrick, G. M. *J. Chem. Soc. A* **1968**, *11*, 2828.
(3) Kouvetakis, J.; Menedez, J.; Chizmeshya, A. V. G. *Annu. Rev. Mater. Res.* **2006**, *36*, 497.
(4) Forsyth, G. A.; Rankin, D. W. H.; Robertson, H. E. *J. Mol. Struct.* **1990**, *239*, 209.
(5) Schumann, H.; Kroth, H. J. *Z. Naturforsch., B: Anorg. Chem., Org. Chem.* **1977**, *23*, 523.
(6) Becker, G.; Hoelderich, W. *Chem. Ber.* **1975**, *108*, 2484.
(7) Buerger, H.; Goetze, U.; Sawodny, W. *Spectrochim. Acta, Part A* **1970**, *26*, 671.
(8) Schulz, S.; Nieger, M. *J. Organomet. Chem.* **1998**, *570*, 275.
(9) Beagley, B.; Robiette, A. G.; Sheldrick, G. M. *Chem. Commun.* **1967**, *12*, 601. Blake, A.; Ebsworth, E. A. V.; Henderson, S. G. D. *Acta Crystallogr., Sect. C* **1991**, *47*, 489.

as discussed below. The $(GeH_3)_3E$ products are obtained as colorless volatile liquids and are readily purified by trap-to-trap fractionation. The GeH_3Br starting material is obtained in nearly quantitative yield by a direct reaction of GeH_4 with Br_2,[10a] and the $[(CH_3)_3Si)]_3E$ (E = P, As, Sb) reagents are synthesized using well-known methods.[10b−d] The ^1H NMR and gas-phase IR data of $(GeH_3)_3E$ are consistent with the proposed structures in which a central P, As, or Sb atom is bonded to three GeH_3 groups. A detailed account of the synthetic procedure and characterization is provided in the experimental section. Density functional theory simulations are used to interpret observed vibrational spectra and provide detailed thermochemical and bonding information about $(Me_3Ge)_3E$ (E = P, As, or Sb) molecules.

Molecular Properties from First Principles

On the basis of our previous successful simulations of germyl-based compounds[11] we employ the B3LYP model chemistry at the 6-311++G(3df,3pd) basis set level for all molecular structure optimizations and subsequent thermochemical analysis. All results were obtained using the Gaussian03 package.[12] For compounds containing Sb atoms the explicit treatment of core electrons using the 6-311++G(3df,3pd) basis set is computationally demanding, and we therefore adopt effective core potentials (ECP) using the LANL2DZ description[13] to remove 46 core electrons from the electronic structure calculation. This approach assumes that core electrons do not contribute to chemical bonding, and thus the associated thermochemical behavior is expected to be unaffected by this simplification. In this study we explicitly verify this notion a posteriori for the lighter compounds $P(GeH_3)_3$ and $As(GeH_3)_3$, by directly comparing the results of ECP calculations with those obtained from a full-core (FC) treatment. The elimination of core electrons also leads to a concomitant reduction in the total molecular electronic energy. Thus reactant and product species containing a given heavy element must be treated on the same footing to obtain free energies of reaction. An example is the formation of trigermyl-stibine from germane and stibine:

$$2SbH_3(g) + 6GeH_4(g) \rightarrow 6H_2(g) + 2Sb(GeH_3)_3(g) \quad (3)$$

Here again our strategy is to establish the reliability of the ECP treatment by comparison of the analogous P- and As-based reactions for which both ECP and FC calculations can be carried out (discussed in detail below).

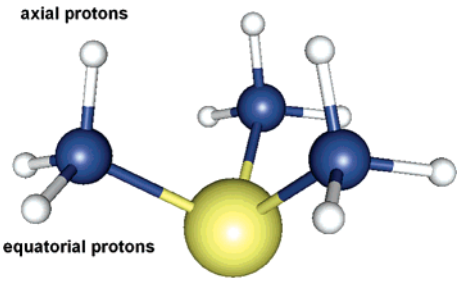

Figure 1. Structure of $M(GeH_3)_3$ molecules indicating the location of axial and equatorial protons. The M atom and Ge atoms are shown as yellow and blue spheres, respectively.

Table 1. Calculated Bond Lengths, Bond Angles, and Torsion Angles for Phosphine, Arsine, and Stibine[a]

molecule		r(M−H)	∠(**H**−M−H)	ϕ(**H**−M−H−H)
PH_3	ECP	1.427	93.40	93.61
	FC	1.418	93.45	93.68
	exptl	1.421	93.50	
AsH_3	ECP	1.525	92.37	92.47
	FC	1.524	92.19	92.27
	exptl	1.519	91.83	
SbH_3	ECP	1.713	91.60	91.65
	FC			
	exptl	1.707	91.30	

[a] Bond Lengths are in angstroms; angles are in degrees. Experimental data are taken from ref 13.

Structural Trends. The detailed molecular structures of $P(GeH_3)_3$, $As(GeH_3)_3$, and $Sb(GeH_3)_3$ molecules are not well-characterized; to our knowledge only gas electron diffraction (GED) determinations of the experimental geometry of $P(GeH_3)_3$ have been made to date.[14,15] The basic structure of the $M(GeH_3)_3$ molecules is illustrated schematically in Figure 1, which also shows the locations of the axial and equatorial protons in relation to the MGe_3 framework. The vibrational spectrum of $P(GeH_3)_3$ has been reported.[15] Because of the scarcity of extant bond length data for the target molecules we have pursued a number of strategies to validate our simulation results. For instance, reliable structure determinations have been reported for phosphine (PH_3), arsine (AsH_3), stibine (SbH_3), and germane (GeH_4). We therefore simulated these molecules as a preliminary gauge of the model chemistry and basis set performance. Table 1 compares their calculated and experimentally determined structures. For phosphine the P−H bond length, 1.427 Å, obtained using the ECP treatment is 0.009 Å greater than that obtained using the more rigorous FC description, while

(10) (a) Swiniarski, M. F.; Onyszchuk, M. *Inorg. Synth.* **1974**, *15*, 157. (b) Becker, G.; Holderich, W. *Chem. Ber.* **1975**, *108*, 2484. (c) Becker, G.; Gutenkunst, G.; Wessely, H. J. *Z. Anorg. Allg. Chem.* **1980**, *462*, 113. Wells, R. L.; Self, M. S.; Johansen, J. D.; Laske, J. A.; Aubuchon, S. R.; Jones, L. J. *Inorg. Synth.* **1997**, *31*, 150. (d) Amberger, E.; Salazar, G. R. W. *J. Organomet. Chem.* **1967**, *8* (1), 111.

(11) Ritter, C. J.; Hu, C.; Chizmeshya, A. V. G.; Tolle, J.; Klewer, D.; Tsong, I. S. T.; Kouvetakis, J. *J. Am. Chem. Soc.* **2005**, *127* (27), 9855−9864. Chizmeshya, A. V. G.; Ritter, C. J.; Hu, C.-W.; Tolle, J.; Nieman, R. A.; Tsong, I. S. T.; Kouvetakis, J. *J. Am. Chem. Soc.* **2006**, *128*, 6919.

(12) Frisch, M. J.; Trucks, G. W.; Schlegel, H. B.; Scuseria, G. E.; Robb, M. A.; Cheeseman, J. R.; Montgomery, J. A., Jr.; Vreven, T.; Kudin, K. N.; Burant, J. C.; Millam, J. M.; Iyengar, S. S.; Tomasi, J.; Barone, V.; Mennucci, B.; Cossi, M.; Scalmani, G.; Rega, N.; Petersson, G. A.; Nakatsuji, H.; Hada, M.; Ehara, M.; Toyota, K.; Fukuda, R.; Hasegawa, J.; Ishida, M.; Nakajima, T.; Honda, Y.; Kitao, O.; Nakai, H.; Klene, M.; Li, X.; Knox, J. E.; Hratchian, H. P.; Cross, J. B.; Bakken, V.; Adamo, C.; Jaramillo, J.; Gomperts, R.; Stratmann, R. E.; Yazyev, O.; Austin, A. J.; Cammi, R.; Pomelli, C.; Ochterski, J. W.; Ayala, P. Y.; Morokuma, K.; Voth, G. A.; Salvador, P.; Dannenberg, J. J.; Zakrzewski, V. G.; Dapprich, S.; Daniels, A. D.; Strain, M. C.; Farkas, O.; Malick, D. K.; Rabuck, A. D.; Raghavachari, K.; Foresman, J. B.; Ortiz, J. V.; Cui, Q.; Baboul, A. G.; Clifford, S.; Cioslowski, J.; Stefanov, B. B.; Liu, G.; Liashenko, A.; Piskorz, P.; Komaromi, I.; Martin, R. L.; Fox, D. J.; Keith, T.; Al-Laham, M. A.; Peng, C. Y.; Nanayakkara, A.; Challacombe, M.; Gill, P. M. W.; Johnson, B.; Chen, W.; Wong, M. W.; Gonzalez, C.; Pople, J. A. *Gaussian 03*, revision B.04; Gaussian, Inc.: Wallingford, CT, 2003.

(13) Arsine referance: http://wulfenite.fandm.edu/Parameters%20table/p-bi_cmpds.htm (The data in this reference are taken from *Tables of Interatomic Distances and Configuration in Molecules and Ions*; Sutton, L. E., Ed.; The Chemical Society: London, 1958).

(14) Rankin, D. W. H.; Robiette, A. G.; Sheldrick, G. M.; Beagley, B.; Hewitt, T. G. *J. Inorg. Nucl. Chem.* **1969**, *31*, 2351.

(15) Beagley, B.; Medwid, A. R. *J. Mol. Struct.* **1977**, *38*, 229.

Table 2. Calculated Bond Lengths, Bond Angles, and Torsion Angles for Germane and the Group V Trigermyl Compounds $P(GeH_3)_3$, $As(GeH_3)_3$, and $Sb(GeH_3)_3$

molecule		*r*(M−Ge)	*r*(Ge−H)	∠(**M**−**Ge**−**H**)	∠(**H**−**Ge**−**H**)	∠(**Ge**−M−Ge)	*φ*(**H**−**Ge**−**H**−M)	*φ*(**H**−**Ge**−M−Ge)
GeH_4	ECP							
	FC		1.533		109.5			
	exptl		1.527		109.5			
$P(GeH_3)_3$	ECP	2.360	1.536	107.9, 112.9	109.3, 109.5	98.9	117.4, 120.4, 123.4	50.3, 70.6, 171.1
	FC	2.340	1.537	108.1, 113.2	109.1, 109.3	98.7	117.2, 120.1, 123.1	50.1, 70.8, 171.1
	exptl	2.306[a]	1.500[a]					
		2.334[b]						
$As(GeH_3)_3$	ECP	2.461	1.537	108.3, 112.7	109.1, 109.2	96.8	117.7, 120.9, 123.3	48.4, 72.5, 169.3
	FC	2.450	1.538	108.4, 112.9	109.1, 109.3	96.1	117.8, 120.9, 123.1	48.4, 72.5, 169.4
	exptl							
$Sb(GeH_3)_3$	ECP	2.655	1.539	109.2, 112.5	108.4, 108.8	93.3	118.8, 121.1, 123.1	46.7, 74.1, 167.6
	FC							
	exptl							

[a] GED measurements from ref 14. [b] Heteronuclear average obtained from Table 3 by averaging P−P and Ge−Ge for P_2H_4 and Ge_2H_6, respectively.

Table 3. Calculated B3LYP/6-311++G(3df,3pd) Bond Lengths, Bond Angles, and Torsion Angles of P_2H_4 and Ge_2H_6[a]

molecule		*r*(M−M)	*r*(M−H)	∠(**M**−M−H)	∠(**H**−M−H)	*φ*(**H**−M−M−H)	*φ*(**H**−M−H−M)
P_2H_4	FC	2.2306	1.4052	95.52	94.56	84.86, 180.00	96.01
	exptl	2.2190	1.4155				
Ge_2H_6	FC	2.4390	1.5372	110.42	108.51	60.00, 180.00	
		2.430[b]	1.5410[b]		106.40[b]		
	exptl	2.448					

[a] The experimental Ge−Ge bond length was derived from bulk crystalline Ge. Average M−M bond length is 2.335 Å (FC calculation) and 2.272 Å (experiment). [b] Theoretical values reported by ref 16.

in arsine the difference is much smaller (0.001 Å). For both phosphine and arsine the bond angle discrepancies between FC and ECP are less than 0.2°. Perhaps fortuitously, the bond lengths calculated using the ECP treatment are *systematically* smaller than the experimental values by ∼0.006 Å, throughout the molecular sequence. However, the corresponding differences in the H−M−H angle (M = P, As, Sb) are underestimated for phosphine and overestimated for arsine and stibine. The FC calculations produce the same H−M−H bond angle trend and also yield an underestimate/overestimate of the M−H bond lengths in phosphine/arsine of 0.003−0.005 Å. When taken collectively the mean deviations between the calculated and observed bond lengths (using either FCs or the ECP approximation) are on the order of 0.005 Å for bond lengths and 0.2° for bond angles.

The calculated structural data for GeH_4, $P(GeH_3)_3$, $As(GeH_3)_3$, and $Sb(GeH_3)_3$ are provided in Table 2, where it is compared with available experimental data. We have obtained ECP and FC results for all group V trigermyl molecules, except for $Sb(GeH_3)_3$ for which only the ECP results were feasible. Since germanium is consistently treated at the FC level in all molecules in which it appears, an ECP treatment was not pursued. As can be seen from the table the B3LYP/6-311++G(3df,3pd) basis set provides an excellent account of the germane molecule's structure (Ge−H bond length greater than the observed value by ∼0.005 Å). For the trigermyl molecules the M−Ge (M = P, As, Sb) bond lengths increase systematically (in steps of ∼0.1 Å) throughout the sequence $P(GeH_3)_3$, $As(GeH_3)_3$, and $Sb(GeH_3)_3$. The primary effect of the ECP approximation is to dilate the M−Ge bond lengths by ∼0.01 Å relative to the FC values. It is also noteworthy that the Ge−H bonds (second neighbors to the central atom) exhibit a concomitant, albeit smaller (∼0.001 Å), systematic expansion.

The bond angles and torsion angles also exhibit systematic changes throughout this sequence. Our simulations indicate that bond angles and bond torsions are essentially independent of the core treatment employed for the central atom. Collectively, the smallest variation (<0.6°) is found in the H−Ge−H angles which exhibit a nearly perfect tetrahedral value, while the largest variations occur in the Ge−M−Ge angles (∼98°, 96°, and 93° in $P(GeH_3)_3$, $As(GeH_3)_3$, and $Sb(GeH_3)_3$, respectively). The Ge−M−Ge bond angle trends may have important implications for the functional incorporation of these molecular units into tetrahedral semiconductors (e.g., substitutional doping in tetrahedral diamond lattice sites). Our calculations predict that the Ge−M−Ge angles move away from the tetrahedral value along the sequence P, As, and Sb suggesting that the most facile incorporation (based on limitation of bond bending) may occur for the PGe_3 molecular core of $P(GeH_3)_3$. However, if the accommodation of the dopant within a predominantly germanium host lattice is controlled by bond length then arsenic incorporation would result in the smallest lattice stress (cf. *r*(As−Ge) = 2.50 Å and *r*(Ge−Ge) ∼ 2.445 Å).

As can be seen from Table 2, the experimental value for the P−Ge bond length in $P(GeH_3)_3$ (2.306 Å) is significantly smaller than the calculated FC value (2.340 Å). This is surprising in view of the excellent agreement between calculated and observed values found for the other compounds discussed above (see Table 1). A plausible independent estimate of the P−Ge bond length can also be obtained by taking the heteronuclear average of P−P and Ge−Ge bond lengths in P_2H_4 and Ge_2H_6 molecules, respectively. Calculated FC structures for these two molecules are compared with available experimental data in Table 3, which indicates excellent agreement in the case of P_2H_4 (bond length errors ∼ 0.01 Å). A similar level of agreement is found for Ge_2H_6, for which, however, the bulk crystalline Ge value (2.448 Å) is listed as a proxy for the molecular value (a reliable GED determination could not be found). The average of the experimental P−P and Ge−Ge values

Table 4. Summary of Observed and Calculated Vibrational Frequencies[a]

		$P(GeH_3)_3$			$As(GeH_3)_3$			$Sb(GeH_3)_3$	
	ref 15	exptl	FC	ECP	exptl	FC	ECP	exptl	ECP
n_8	2080	**2079**	2072	2079	**2077**	2074	2076	**2071**	2075
n_7	2064	**2062**	2063	2068	**2063**	2060	2061	**2060**	2060
n_6		**2053**	2051	2051	**2055**	2052	2052	**2055**	2053
n_5	875	**872**	882	883	**874**	881	882		
	869	**870**	874	875	**869**	875	876	**864**	887
n_4	839	**839**	840	840	**829**	830	832		883
								838	821
								826	
								814	
n_3	798	**799**	795	793	**785**	784	783	**797**	773
	756	**753**						**768**	
n_2	563	**558**	556	555	**529**	520	523		
n_1	514	**516**	502	505	**490**	478	479	**486**	485
		367	359	358				**457**	446
		327	299	301		258	258		210
		112							
		100	93	82		76	63		64
		88	74	71		63	54		55

[a] Column labeled "exptl" is data obtained in the present study (entries are in bold font), while FC and ECP refer to FC and ECP calculations, respectively. All theoretical frequencies above 2000 cm^{-1} include a scale factor of 0.976.

yields 2.334 Å, which is essentially identical to the value obtained by averaging the *calculated* P−P and Ge−Ge bond lengths (2.335 Å). The heteronuclear average value 2.334 Å obtained in this way is much more consistent with the calculated P−Ge bond length (2.340 Å) in the $P(GeH_3)_3$ molecule than the GED value 2.306 Å reported.[14] One possible reason for the discrepancy is the presence of impurities in the synthetic product described in ref 14. This would offset the structural parameters obtained from the GED refinement.

Vibrational Spectra. To complement and interpret the observed infrared spectra of the group V trigermyl compounds we calculated the infrared vibrational frequencies and intensities at the B3LYP/6-311++G(3df,3pd) level for $P(GeH_3)_3$ and $As(GeH_3)_3$. Since the $Sb(GeH_3)_3$ molecule could only be treated using ECPs we also carried out analogous ECP calculations for the lighter molecules in the sequence, for which the quality of the calculated spectra could be compared with a FC treatment. No symmetry was imposed in the calculation of the frequency spectra, and all molecules studied exhibited a positive definite spectrum of harmonic frequencies indicating that the ground state structures are dynamically stable for both the all-electron and the ECP treatment. Below 1500 cm^{-1} the spectra of $P(GeH_3)_3$ and $As(GeH_3)_3$ obtained from FC and the ECP approximation were indistinguishable [see Table 4] while in the Ge−H stretch range (2000−2200 cm^{-1}) all bands obtained from FC treatment are shifted downward (rigidly) by ∼8 cm^{-1} (further details are provided below).

Figures 2−4 show plots of the calculated spectra of $P(GeH_3)_3$, $As(GeH_3)_3$, and $Sb(GeH_3)_3$, respectively, convoluted with a Gaussian of width ∼20 cm^{-1} to simulate experimental broadening. Both the high- and low-frequency regions are shown. No frequency scaling was applied to the low-frequency spectra while a factor of 0.976 derived from our prior work on germyl compounds[11] was applied to the high-frequency portion of the calculated spectra which are

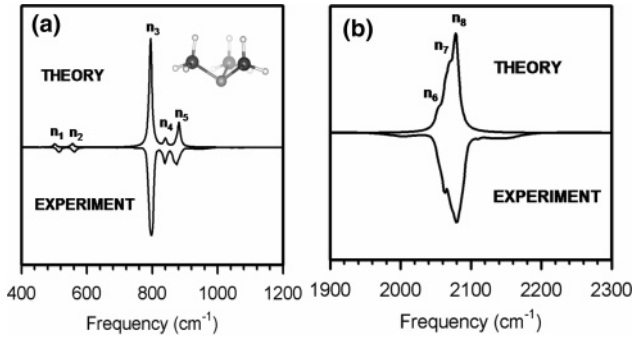

Figure 2. Comparison of the experimental and (all-electron) theoretical spectra of $P(GeH_3)_3$: (a) low-frequency region (400−1200 cm^{-1}) and (b) high-frequency Ge−H region (1900−2300 cm^{-1}). A frequency scale factor of 0.976 was applied to the high-frequency theoretical spectrum

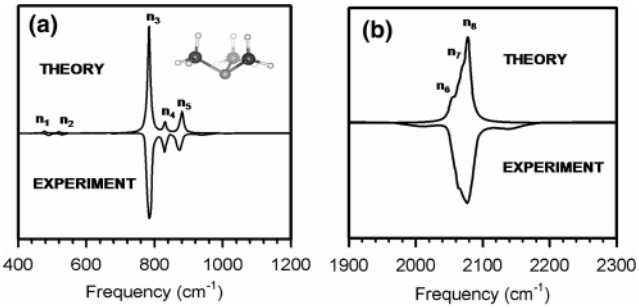

Figure 3. Comparison of the experimental and (all-electron) theoretical spectra of $As(GeH_3)_3$: (a) low-frequency region (400−1200 cm^{-1}) and (b) high-frequency Ge−H region (1900−2300 cm^{-1}). A frequency scale factor of 0.976 was applied to the high-frequency theoretical spectrum.

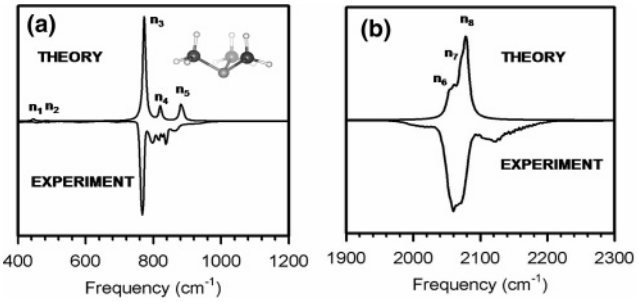

Figure 4. Comparison of the experimental and (all-electron) theoretical spectra of $Sb(GeH_3)_3$: (a) low-frequency region (400−1200 cm^{-1}) and (b) high-frequency Ge−H region (1900−2300 cm^{-1}). A frequency scale factor of 0.976 was applied to the high-frequency theoretical spectrum.

comprised of Ge−H stretching vibrations. For simplicity the same scale factor was applied to both the FC [$P(GeH_3)_3$, $As(GeH_3)_3$] and the ECP [$Sb(GeH_3)_3$] calculations. Note the excellent agreement between the calculated and the experimental spectra in Figures 2 and 3. For $Sb(GeH_3)_3$ in Figure 4, the presence of additional very weak peaks is likely due to minor decomposition of the compound.

All experimental and calculated vibrational spectra are summarized in Table 4. The principal features in the low- and high-frequency spectra of all compounds are labeled n_1−n_8 and are assigned as follows. The relatively weak features labeled as n_1 and n_2 involve transverse and radial in-phase wagging of the axial germyl group protons (see Figure 1), respectively. The transverse central atom vibrations (not shown in the plots because of instrumental detection limit) occur below 400 cm^{-1} and have frequencies ∼360 cm^{-1}, ∼260 cm^{-1}, and ∼205 cm^{-1} for $P(GeH_3)_3$, $As(GeH_3)_3$, and $Sb(GeH_3)_3$, respectively. The most intense low-frequency

Table 5. All Electron (FC) Thermochemical Data Calculated at the B3LYP/6-311++G(3df,3pd) Level[a]

	E_0		$E_0 + \Delta H$		$E_0 + \Delta G$	
molecule	FC	ECP	FC	ECP	FC	ECP
H_2	−1.1800		−1.1667		−1.1815	
GeH_4	−2079.4068		−2079.3735		−2079.3982	
PH_3	−343.1797	−8.2998	−343.1520	−8.2726	−343.1758	−8.2965
AsH_3	−2237.6769	−7.9201	−2237.6512	−7.8946	−2237.6765	−7.9198
SbH_3		−7.1887		−7.1655		−7.1919
$P(GeH_3)_3$	−6577.8553	−6242.9800	−6577.7725	−6242.8982	−6577.8219	−6242.9465
$As(GeH_3)_3$	−8472.3702	−6242.6099	−8472.2880	−6242.5287	−8472.3395	−6242.5786
$Sb(GeH_3)_3$		−6241.8895		−6241.8076		−6241.8599

[a] Columns list the electronic ground state energy (E_0), as well as corresponding values corrected for enthalpy (ΔH) and free energy (ΔG). All values are listed in hartree.

Table 6. Reaction Free Energies for the Gas Phase Formation of the Germyl Compounds from Their Hydrides Following Equation 4[a]

formation reaction	ΔG(0 K) (kJ/mol)	ΔG(298 K) (kJ/mol)
$P(GeH_3)_3$ (FC)	−275	−21
$P(GeH_3)_3$ (ECP)	−251	−1
$As(GeH_3)_3$ (FC)	−186	68
$As(GeH_3)_3$ (ECP)	−204	46
$Sb(GeH_3)_3$ (ECP)	−158	94

[a] Results are given in kJ/mol.

peak in the spectrum of all three molecules is designated as n_3 and involves asymmetrical in-phase transverse motion of both axial and equatorial protons with respect to the molecule's center of mass. The remaining two low-frequency features, denoted by n_4 and n_5, are assigned as concerted symmetrical radial wagging of axial and equatorial protons and symmetrical wagging of the axial protons parallel to the Ge plane, respectively.

Molecular Stability and Thermochemical Properties. To estimate the *relative* thermodynamic stability of the $P(GeH_3)_3$, $As(GeH_3)_3$, and $Sb(GeH_3)_3$ compounds we consider their free energy of formation from germane and the corresponding hydrides PH_3, AsH_3, and SbH_3, according to

$$2MH_3(g) + 6GeH_4(g) \rightarrow 6H_2(g) + 2M(GeH_3)_3(g) \quad (M = P, As, Sb) \quad (4)$$

Table 5 lists the thermochemical energies of all molecules, calculated using FC (FC) and the ECP approximation, respectively, including the total ground state electronic energy E_0, as well as E_0 corrected for enthalpy (ΔH) and free energy (ΔG) at 298 K. Because the antimony-based reactions could only be calculated on the basis of the ECP approximation we carried out control calculations for the analogous P- and As-based reactions at both the ECP and the FC levels. Our main results are summarized in Table 6, which lists the free energy differences for the reaction in eq 4 obtained using FC and ECP approximations. All three trigermyl compounds ($P(GeH_3)_3$, $As(GeH_3)_3$, and $Sb(GeH_3)_3$) are predicted to be stable at low temperature, but only the trigermyl-phosphine is predicted to be thermodynamically stable at room temperature. For this compound the FC treatment predicts larger free energies than the ECP approximation, while for trigermyl-arsine we find the reverse. Nevertheless, both FC and ECP treatments predict that trigermyl-stibine is the least favored product followed by the trigermyl-arsine and then the phosphorus analog. In the following sections we describe initial proof-of-concept As doping experiments of metastable Ge-rich semiconductor films using $As(GeH_3)_3$.

Synthesis of As-Doped $Ge_{1-y}Sn_y$ Films

The facile reactivity of the $As(GeH_3)_3$ compound prompted us to pursue low-pressure CVD of As-doped $Ge_{1-y}Sn_y$ films at 300−350 °C. The unimolecular decomposition of the molecule proceeds readily on Si(100) at temperatures as low as 350 °C to form thin Ge−As films with approximately 30 atom %, suggesting that the entire Ge_3As molecular core could be incorporated into the solid. Here we concentrate on samples with As concentrations within the typical range for device applications of $\sim 10^{18}-10^{19}$ atoms/cm^3 (0.002%−0.02% based on the density of elemental Ge). These doped $Ge_{1-y}Sn_y$ films were routinely obtained on Si(100) via reactions of appropriate amounts Ge_2H_6, SnD_4, and $As(GeH_3)_3$ and were characterized using a broad range of methods including spectroscopic ellipsometry to determine the electrical properties. In a typical experiment, the Si(100) substrates were prepared by a modified RCA process followed by hydrogen passivation of the surface using a 10% HF solution. The Ge_2H_6, SnD_4, and $As(GeH_3)_3$ reactants were regulated using mass flow controllers and introduced into the growth chamber, perpendicular to the substrate surface. Precise control of the As content in the samples was achieved by varying the partial pressure of the gaseous sources in the reaction mixture. The duration of a deposition was typically 30 min. The reactor base pressure was 10^{-9} Torr rising to ∼0.3 Torr during growth. The films were examined by Rutherford backscattering (RBS) to determine the ratio of Ge to Sn. Furthermore, a comparison of the random and aligned spectra (see Figure 5a) shows nearly perfect ion (He^{2+}) channeling by Ge and Sn, indicating that the elements occupy diamond lattice sites (complete substitutionality). Since we cannot resolve the As signal using RBS due to the similarity in atomic mass with Ge, we utilized particle induced X-ray emission (PIXE) and secondary ion mass spectrometry (SIMS) to show that the films contained As and to qualitatively estimate its content (see Figure 5b). The precise As elemental content was quantified by a more detailed SIMS analysis using bulk Ge standards of known As concentrations. In order to get a sufficient intensity signal for the ^{75}As in the Ge standard and to diminish mass interference of possible $^{74}Ge-H$ species the primary Cs^+ beam had to be set at 14.15 keV. The depth dependence of the signal intensity for the Ge standard (3.1×10^{19} As atoms/cm^3) was corrected below 10 nm to account for anomalies created during the initial sputtering of the sample. All subsequent samples were corrected in the same fashion and exhibit highly uniform depth profiles of the constituent

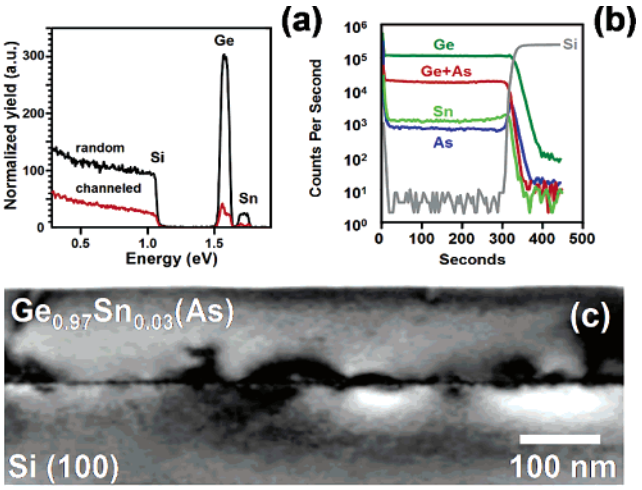

Figure 5. (a) RBS of the $Ge_{0.97}Sn_{0.03}$(As)/Si(100) layer (random and aligned traces: black and red, respectively), (b) SIMS elemental profile of $Ge_{0.97}$-$Sn_{0.03}$ containing a highly uniform As concentration throughout the sample, and (c) bright field XTEM micrograph of the $Ge_{0.97}Sn_{0.03}$(As)/Si(100) layer.

elements, Ge, Sn, and As, throughout the layers. When the standard was used as a reference, the As contents of two samples with a nominal RBS composition of $Ge_{0.97}Sn_{0.03}$ were found to be 2.3×10^{19} and 2.1×10^{19} atoms/cm^3.

To further evaluate the samples for potential device applications we characterized their microstructure and morphology by cross-sectional transmission electron microscopy (XTEM), high-resolution X-ray diffraction (HRXRD), and atomic force microscopy (AFM). Figure 5c shows a bright field XTEM micrograph of the entire thickness for a representative $Ge_{0.97}Sn_{0.03}$(As)/Si(100) film showing high uniformity, a flat surface, and no threading dislocation penetrating to the surface within the field of view, despite the large mismatch in lattice dimensions. Generally we find that defects are concentrated near the film/substrate interface region while the upper portion of the layer remains relatively defect-free. High-resolution micrographs of the interface in (110) projection revealed nearly perfect commensuration of the (111) lattice planes. The AFM root-mean-square values are ~0.7 nm for areas of 5×5 μm^2 indicating a smooth film surface consistent with the XTEM observations.

HRXRD reciprocal space maps indicate single-phase, monocrystalline material with a completely strain-relaxed microstructure. Figure 6 shows the (004) and the off-axis (224) reciprocal space maps of the $Ge_{0.97}Sn_{0.03}$(As)/Si(100) heterostructure acquired with a Panalytical X'Pert MRD XRD system. Note that the line connecting the Si(224) peak with the spectrum origin passes precisely through the center of the off-axis diffraction spot of the film indicating perfect relaxation with respect to silicon. The lattice parameter in the growth direction ($a_{\perp,GeSn} = 5.685$ Å) is virtually identical to the in-plane counterpart, parallel to the interface ($a_{||,GeSn} = 5.683$ Å), indicating perfect cubic structure devoid of any strain-induced tetragonal distortions. This is consistent with the lattice expansion due to the incorporation of the larger Sn atoms in the tetrahedral Ge structure ($a_{Ge} = 5.657$ Å). The X-ray measurements reveal a lateral grain size of approximately ~5275 Å and a mosaic spread of 0.288° indicating highly aligned crystal domains.

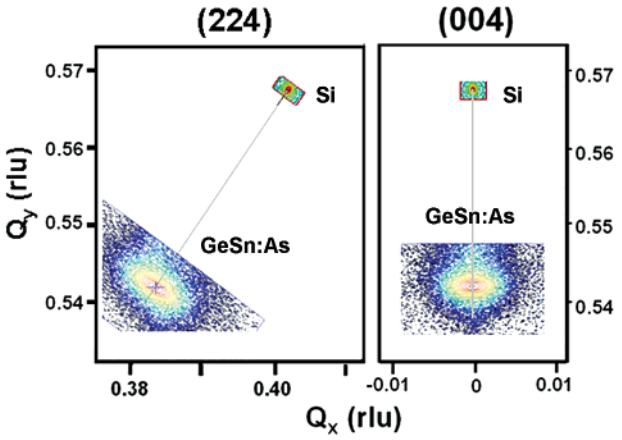

Figure 6. High-resolution triple axis XRD reciprocal space maps of the (224) and (004) Bragg reflections of the film indicating a completely strain free material. Reciprocal lattice units (rlu) are employed in which $Q_x = \lambda\sqrt{8}/2a_{||}$ ($\lambda = 1.54$ Å) and $Q_x = 2\lambda/a_{\perp}$.

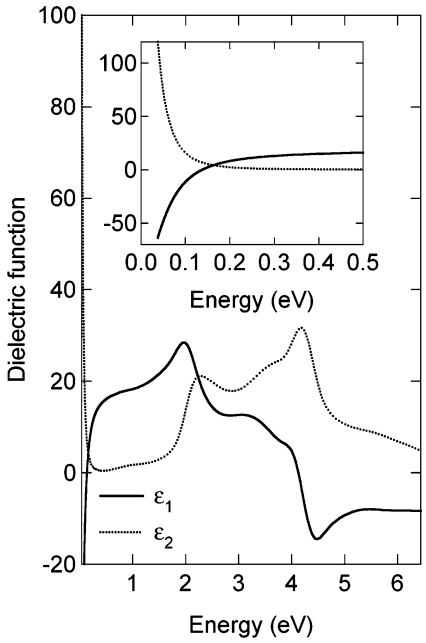

Figure 7. Real (solid line) and imaginary (dotted line) parts of the dielectric function of a $Ge_{0.97}Sn_{0.03}$:As sample at room temperature obtained with spectroscopic ellipsometry. The inset shows in more detail the metallic Drude-like response of the free carriers in the infrared. Modeling the metallic contribution with eq 5, we obtain for this sample $\rho_0 = 0.0124$ Ω cm and $\tau = 1.14 \times 10^{-14}$ s.

Ellipsometric Characterization. We have used spectroscopic ellipsometry to monitor the free carriers using a contactless optical method. The equipment and the methodology used to analyze the data is the same as in ref 17. Figure 7 shows the measured dielectric function of $Ge_{1-y}Sn_y$:As. The low-energy divergence, shown more clearly in the inset, is due to the metallic response of the free electrons, and it can be modeled by adding to the dielectric function a Drude-like expression

(16) Urban, J.; Schreiner, P. R.; Vacek, G.; Schleyer, P. v. R.; Huang, J.; Leszczynski, J. *Chem. Phys. Lett.* **1997**, *264*, 441.
(17) D'Costa, V. R.; Cook, C. S.; Birdwell, A. G.; Littler, C. L.; Canonico, M.; Zollner, S.; Kouvetakis, J.; Menendez, J. *Phys. Rev. B* **2006**, *73*, 125207.

$$\epsilon_{\text{Drude}}(\omega) = -\frac{4\pi}{\rho_0(\omega^2\tau + i\omega)} \quad (5)$$

where ω is the angular frequency, ρ_0 is the DC resisitivity, and τ is the relaxation time. The parameters ρ_0 and τ are obtained from fits to the data. The carrier concentration n can be obtained from the fit parameters ρ_0 and τ using

$$n = \frac{m^*}{\rho_0 e^2 \tau} \quad (6)$$

where m^* is the conductivity effective mass and e is the electron charge. Since the electronic structure of our $Ge_{1-y}Sn_y$ alloys is Ge-like (see Figure 8), we expect the electrons to reside in the conduction band L-valleys along the ⟨111⟩ direction of the Brillouin zone. The effective mass for these valleys in $Ge_{1-y}Sn_y$ alloys has not been measured, but since in our samples $y = 0.03$, we tentatively use the effective mass in pure Ge. For n-type Ge it is known that an effective mass $m^* = 0.14m_e$ (where m_e is the electron mass) leads to good agreement between infrared reflectivity, Raman scattering, and electrical measurements that use a Hall factor $\gamma_H = 1$ for carrier concentration determinations.[18] We have confirmed that this agreement remains excellent if one employs spectroscopic ellipsometry instead of infrared reflectivity or Raman scattering. The three circles in Figure 9 give the resistivity versus carrier concentration for three As-doped Ge samples. These quantities were determined from ellipsometry using $m^* = 0.14m_e$. We note that the three data points agree exceedingly well with the solid line in Figure 9, which corresponds to the electrical measurements of Cuevas and Fritzsche[19] and Spitzeret al.[20,21] If we use the same effective mass for $Ge_{0.97}Sn_{0.03}$:As, we obtain carrier concentrations of 3.05×10^{19} cm^{-3}, 3.45×10^{19} cm^{-3}, and 5.26×10^{19} cm^{-3} for the three representative samples described here. These values are *higher* than the As concentrations determined from SIMS measurements. Carrier concentrations *smaller* than dopant atom concentrations can be understood in terms of incomplete dopant activation, but there is no simple explanation for the opposite behavior. Figure 9 shows the resistivity versus carrier concentration as measured with ellipsometry (solid squares) and the same resistivity versus the As-concentration from SIMS (empty squares) for our $Ge_{0.97}Sn_{0.03}$:As samples. (Unfortunately, the sample with the highest carrier concentration is too thin for SIMS measurements.). We note that the data points are closer to the Ge curve if we use the concentrations from SIMS. The agreement can be made even better (see dotted line in Figure 9) if we assume that alloy scattering contributes a mobility of the form (in cm^2/(V s)) $\mu_{\text{alloy}} = 26.2(300\text{K}/T)^{0.8}/y(1-y)$, which we obtain by scaling the measured alloy scattering mobility in Ge-rich $Ge_{1-x}Si_x$ alloys,[22] assuming

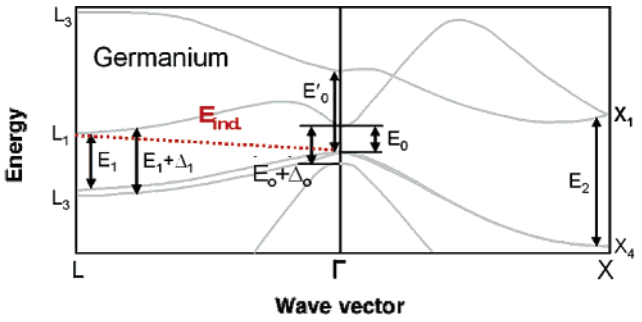

Figure 8. Ge-like band structure in the vicinity of the fundamental gap. The diagram shows the measured optical transitions and the indirect gap.

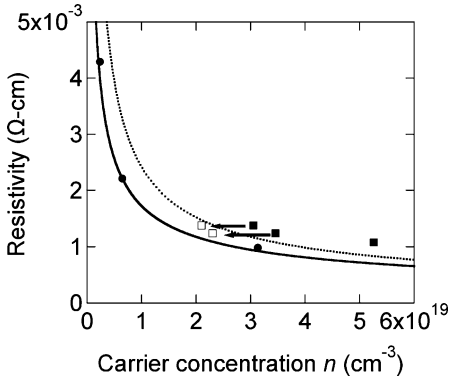

Figure 9. Circles represent the resistivity versus carrier concentration in three Ge:As samples, as obtained from spectroscopic ellipsometry. The carrier concentration was computed using $m^* = 0.14m_e$. The solid line corresponds to the electrical measurements in refs 19−21 assuming a Hall factor $\gamma_H = 1$. Squares show the resistivity (from ellipsometry) for three $Ge_{0.97}Sn_{0.03}$ samples. Solid squares use a carrier concentration determined from ellipsometry using $m^* = 0.14m_e$. Empty squares assume that the carrier concentration is equal to the As concentration measured by SIMS. The dotted line is the calculated resistivity if one considers the contribution from alloy scattering as discussed in the text.

that the scattering potential is proportional to the electronegativity difference.

An effective mass $m^* = 0.094m_e$ would bring the ellipsometric and SIMS measurements of the As concentration into agreement. To investigate this possibility we have calculated the compositional dependence of the effective mass using the theory of Cardona et al.[23] and the recently measured compositional dependence of the E_1 and $E_1 + \Delta_1$ gaps in $Ge_{1-y}Sn_y$ alloys.[17] For Ge at room temperature and a carrier concentration of 4×10^{19} cm^{-3}, the calculated effective mass is $m^* = 0.135m_e$. This is close to the value ($m^* = 0.14m_e$) we found to give excellent agreement between electric and ellipsometric measurements. (Interestingly, if we replot the Ge data in Figure 9 using $m^* = 0.135m_e$ and a Hall factor $\gamma_H = 0.92$ (refs 24 and 25), instead of $m^* = 0.14m_e$ and $\gamma_H = 1$, we maintain the excellent agreement between electric and ellipsometric measurements). The same theory of Cardona et al.[23] predicts for $Ge_{0.97}Sn_{0.03}$ $m^* = 0.131m_e$ so that the calculated mass reduction is far too small to explain the discrepancy between ellipsometry and SIMS in $Ge_{0.97}Sn_{0.03}$:As. There is however an intriguing possibility: recent work suggests that for a Sn concentration of about 3% the difference between the L- and the Γ-minima in the

(18) Cerdeira, F.; Mestres, N.; Cardona, M. *Phys. Rev. B* **1984**, *29*, 3737.
(19) Cuevas, M.; Fritzsche, H. *Phys. Rev. A* **1965**, *139*, 1628.
(20) Spitzter, W. G.; Trumbore, F. A.; Logan, R. A. *J. Appl. Phys.* **1961**, *32*, 1822.
(21) The solid line in Figure 9 is a fit of the electrical measurements with an expression of the form $\rho = [1 + (n/n_0)^{1/2}]/(e\mu_0 n)$. The fit parameters are $\mu_0 = 3000$ cm^2/(V s) and $n_0 = 1.878 \times 10^{17}$ cm^{-3}. The original expression is from Hilsum, C. *Electron. Lett.* **1974**, *10*, 259.
(22) Glicksman, M. *Phys. Rev.* **1958**, *111*, 125.
(23) Cardona, M.; Paul, W.; Brooks, H. *Helv. Phys. Acta* **1960**, *1960*, 329.
(24) Miyazawa, H.; Maeda, H. *J. Phys. Soc. Jpn.* **1960**, *15*, 1924.
(25) Fischetti, M. V.; Laux, S. E. *J. Appl. Phys.* **1996**, *80*, 2234.

conduction band is reduced to 100 meV. On the other hand, if we assume that only the *L*-valleys are occupied, the Fermi level at room temperature is as high as 40 meV for a carrier concentration $n = 2.3 \times 10^{19}$. This means that the Fermi level is only 60 meV $\sim 2k_B(300\ K)$ below the Γ-point valley. A small error in the Sn concentration or in the proposed compositional dependence of the direct and indirect gaps in $Ge_{1-y}Sn_y$ alloys could make this value even smaller, leading to a partial occupation of the Γ-point valley, which has a small effective mass $m^* = 0.04m_e$. Such a scenario, which requires additional work for its confirmation, would provide a natural explanation for the effective mass $m^* = 0.094m_e$ needed to bring ellipsometric and SIMS measurements into agreement, since this mass should be a weighted average of the *L*-valley mass $m^* = 0.14m_e$ and the Γ-valley mass $m^* = 0.04m_e$. This type of measurement may thus shed light on the important issue of measuring the crossover between direct and indirect band gaps in $Ge_{1-y}Sn_y$ alloys.

Simulation of Doped Ge-Rich Films. As discussed in the introduction above, the structural and electronic effects of substitutional P, As, and Sb donor impurities in bulk Ge and SnGe alloys are of considerable practical interest. In the context of the present work on the structure of $M(GeH_3)$ {M = P, As, Sb} molecular hydrides, a detailed understanding of the configuration of "MGe_3" molecular cores ensconced within the parent semiconductor lattice is also highly desirable. For instance, the placement of a Group V dopant on a crystalline Ge site (e.g., substitution) implies an increase in the coordination of M atoms from 3-fold in the gas-phase $M(GeH_3)_3$ molecules discussed above, to a 4-fold "tetrahedral" crystalline coordination state. While this overbonding is qualitatively expected to produce weakened (dilated) M−Ge bonds a detailed quantitative approach is needed to correlate specific bonding changes with the resultant lattice strain. For instance, what is the fate of the lone-pair bonds on the group V dopant atom sites? These questions motivated us to extend our first principles studies to the crystalline setting in order to elucidate both the coordination chemistry of embedded dopant cores as well as the relaxation of the parent lattice associated with the introduction of dopant atoms.

All bulk-phase calculations were performed using density functional theory within the generalized gradient approximation (GGA)[26] as implemented in the Vienna *Ab Initio* Simulation Package (VASP).[27] The electronic wave functions are expanded in a plane wave basis up to a kinetic energy of 37 Ry, and integrations over the first Brillouin zone are performed using discrete summation over a finite number of *k* points. We use a standard Monkhorst−Pack grid[28] (3 × 3 × 3 sampling mesh), which is reduced by symmetry to an irreducible set of four *k*-points in all of our calculations. Projected augmented wave (PAW) pseudopotentials[29] supplied with the VASP code were used in all calculations. However, to improve the fidelity of the simulations 14 valence electrons ($3d^{10}4s^24p^2$) are explicitly included in our treatment of Ge (the dominant species), while only the last five electrons are described by the P, As and Sb pseudopotentials.

Table 7. Calculated Properties of Bulk Phases of Ge, P, As, and Sb[a]

	lattice parameter	μ_A (eV)	ΔE_{SPIN} (eV)	E_C (eV)
Ge	$a = 5.758$ (5.657)	−4.491	−0.723	3.77 (3.86)[e]
P	$a = 3.31$ (3.31)[b]	−5.362	−1.779	3.58 (3.43)[e]
	$b = 11.06$ (10.50)[b]			
	$c = 4.54$ (4.38)[b]			
As	$a = 3.831$ (3.76)[c]	−4.708	−1.593	3.20 (3.13)[e]
	$c = 10.652$ (10.55)[c]			
Sb	$a = 4.404$ (4.31)[d]	−4.172	−1.339	2.83 (2.74)[e]
	$c = 11.293$ (11.27)[d]			

[a] The table lists the lattice parameters, chemical potential, μ_A, spin-density correction (per atom), ΔE_{SPIN}, and cohesive energies, E_C, in eV. The lattice constants for As and Sb correspond to a tripled hexagonal cell setting. (Note: 1 eV = 96.485 kJ/mol.) Experimental values are in parentheses. [b] Reference 30. [c] Reference 31 [d] Reference 32. [e] Reference 33.

The free energies of formation of the doped Ge systems are calculated from the formula $\Delta G_f = E - \sum_k N_k\mu_k$ where *E* is the energy of the doped Ge system (a 64-atom supercell in our case) and N_k and μ_k are the number of atoms of species *k* and their corresponding bulk chemical potential, respectively. We therefore computed the ground state structures of bulk diamond phase Ge, orthorhombic (black phosphorus) P, and rhombohedral As and Sb, as well as their corresponding bulk chemical potentials and cohesive energies. Since all energies produced by the VASP code use nonspin polarized atoms as a reference state we also have calculated the spin polarization energies, ΔE_{SPIN}, required to correct the crystalline ground state energies. Table 7 lists the optimized lattice constants, spin-polarization corrections, chemical potentials, and cohesive energies as well as experimental values for the structural parameters and cohesive energies. The calculated lattice constants are slightly larger than those found experimentally (mean errors of ∼ 2−3%), as commonly observed using the PAW-GGA treatment, while the cohesive energy errors are on the order of ∼0.1 eV (∼9.65 kJ/mol).

We then studied the lattice relaxation induced in a Germanium lattice by dopant atoms by adopting a 64-atom cell representation in which the central atom is replaced by one of P, As, or Sb to yield a concentration of 1.6 atom %. Our use of pure Ge as a proxy for the actual Sn−Ge alloy is a simplification since the Sn concentration is in fact comparable to that of the dopants in our model. Nevertheless it provides a context for the initial study with regards to the *trends* in the behavior along the group V dopant atom sequence. In all cases considered below the cell volume, cell shape, and all atomic positions are simultaneously optimized using stringent criteria to yield a force convergence of 0.001 eV/Å on atoms and a corresponding residual external cell stress of 0.01 kbar. As a test, we optimized the structure of pure germanium by initializing the calculations using randomly perturbed (∼0.2 Å) atomic positions and a slightly orthorhombic supercell. The converged structure produced a cubic cell with lattice constant 11.5163 Å, with all atoms located on diamond lattice sites. The corresponding crystallographic lattice constant, 5.758 Å, compares well with the experimental value 5.658 Å, and the slight 1.7% overestimate is associated with the use of the GGA (we note in passing

(26) Perdew, J. P.; et al. *Phys. Rev. B* **1992**, *46*, 6671.
(27) Kresse, G.; Furthmuller, J. *Comput. Mater. Sci.* **1996**, *6*, 15.
(28) Monkhorst, H. J.; Pack, J. D. *Phys. Rev. B* **1976**, *13*, 5188.
(29) Blöchl, P. E. *Phys. Rev. B* **1994**, *50*, 17953.

Table 8. Comparison of Calculated Ge−M Bond Length Differences with Respect to Ge−Ge in Molecular and Bulk Periodic Settings[a]

	Ge−Ge	Ge−P	Ge−As	Ge−Sb
molecular bond	2.449	2.360	2.461	2.655
% dev from Ge−Ge		−3.6%	+0.5%	+8.4%
defect bond (bulk)	2.494	2.456	2.553	2.662
% dev from Ge−Ge		−1.5%	+2.4%	+6.7%

[a] the molecular bond trends were obtained using the ECP-LANL2DZ treatment while the PAW-GGA was used in the bulk simulations.

that this discrepancy is reduced to a more typical value of 0.6% if the $4s^24p^2$ valence configuration is adopted in the PAW treatment, while otherwise following the same computational procedures).

Using the above approach we find that Ge(P), Ge(As), and Ge(Sb) supercells all exhibit tensile strain (+0.03%, +0.18%, and +0.41%, respectively) relative to pure Ge. While this trend is compatible with the increasing size of the M atoms in the series {P, As, Sb}, the positive strain value for Ge(P) is unexpected on the basis of the molecular bonding trends, since the P atom is "smaller" than Ge. In particular, as shown in Table 8, the LANL2DZ-ECP description yields $b_{GeGe} = 2.449$ Å, $b_{GeP} = 2.360$ Å, $b_{GeAs} = 2.461$ Å, and $b_{GeSb} = 2.655$ Å for Ge_2H_6, $P(GeH_3)_3$, $As(GeH_3)_3$, and $Sb(GeH_3)_3$ molecules, respectively. Thus, the Ge−M single bonds are −3.6%, +0.49%, and +8.4% shorter/longer than Ge−Ge in the molecular setting. As shown in Table 8, a systematic analysis of the bond lengths surrounding the M atoms in the bulk Ge(M) indicates a very similar trend.

An important feature of fully tetrahedrally bonded bulk systems is the average bond strain is identical to the macroscopic lattice strain. Thus, *local bond-strain distributions* within the lattice must account for the difference between the local strain near the dopant site and the strain calculated from the cell dimensions. To verify this notion we examined the variations in bond length in relation to a pure Ge lattice, using the following prescription. With the origin defined at the impurity atom site we loop overall bonds in the supercell and record, as a histogram, the radial distance to each bond center as well as deviation of the local bond length from that in pure Ge. Note that the resulting distribution is independent of the individual bond orientations.

Figure 10 shows a plot of the calculated bond length differences for each M atom. For simplicity the radial distances used in the plots correspond to those of pure Ge. The plots clearly reveal the existence of significant bond-length fluctuations throughout the lattice and that these distributions are different for each guest species. Each panel of Figure 10 reports the average bond length, calculated as an arithmetic mean over all the bond lengths in the cell, as well as the average bond strain taken as a deviation relative to the bond length in pure bulk Ge. In the case of phosphorus doping our simulations predict that the net bond strain is *slightly positive* in spite of the negative deviation at the dopant site, indicating that distant neighbor shells harboring positive bond deviations provide an important compensating effect. We have verified that this result is robust with respect to the extent of the supercell used to model the impurity by performing a full structural lattice relaxation in a larger 256-atom tetragonal cell (4 × 4 × 2 supercell). As can be seen

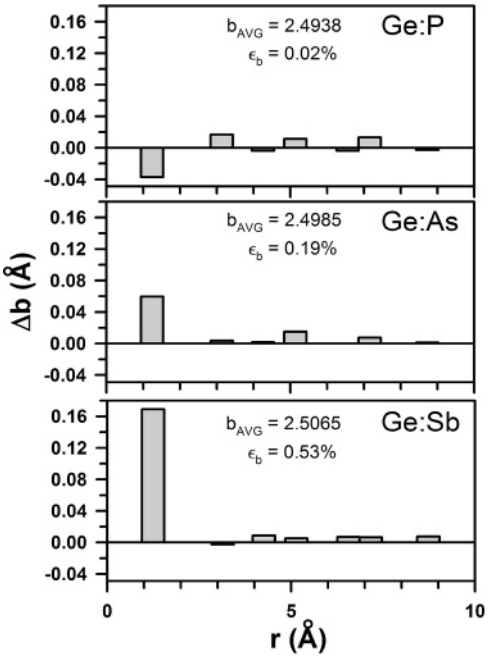

Figure 10. Bond length distortions (relative to pure Ge) as a function of radial distance from the dopant atom. The average bond lengths (b_{AVG}) and corresponding bond strain (ϵ_b) are inset.

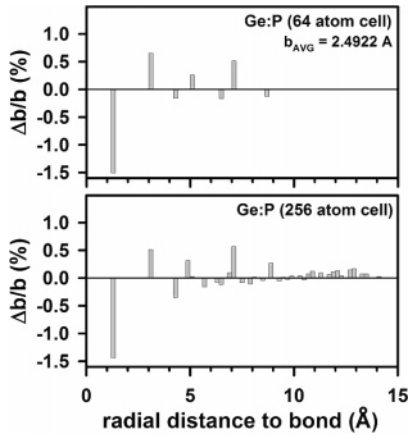

Figure 11. Bond length distortions (relative to pure Ge) as a function of radial distance from the dopant atom.

Table 9. Formation Free Energies, Mean Local Bond Strain $\langle \Delta b/b_{Ge} \rangle$, Lattice Strain $\Delta a/a_0$, and Volume Strain $\Delta V/V_0$ of P-, As-, and Sb-Doped Ge

	ΔG_f (eV)	$\langle \Delta b/b_{Ge} \rangle$	$\Delta a/a_0$	$\Delta V/V_0$
Ge:P	+0.312	0.02%	0.03%	0.09%
Ge:As	+0.308	0.19%	0.17%	0.50%
Ge:Sb	+0.561	0.53%	0.41%	1.22%

from Figure 11, where the distributions for the 64- and 256-atom models are compared, the results are quantitatively very similar indicating that the 64-atom setting provides a realistic representation of the lattice relaxations. As shown in Figure 10, the mean bond strain increases systematically when As and Sb are incorporated into the Ge lattice. For As and Sb dopant sites the first nearest neighbor Ge coordination shells expand to accommodate their larger size while the bond length deviations in subsequent shells (e.g., second and third nearest neighbor) are comparatively small and generally positive. The results are summarized in Table 9 which indicates that the mean bond strains (+0.02%, +0.19%, and 0.53% for Ge(P), Ge(As), and Ge(Sb)) closely match the

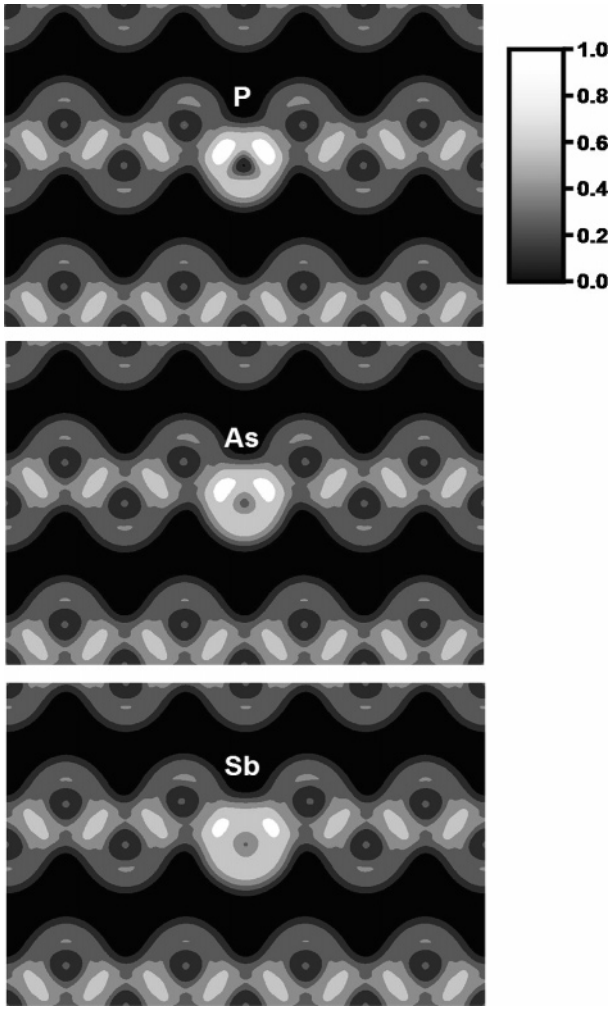

Figure 12. ELF plots in the [110] plane of the 64-atom supercell centered on the dopant atom sites. The dimensions of the panels are $2\sqrt{2}a \times 2a$ (a = lattice parameter).

lattice strain calculated from the equilibrium volume dimensions of the supercells (+0.03%, +0.18%, and +0.41%, respectively).

Finally, in order to elucidate the origin of the stability of the group-V dopant atoms within the tetrahedral bonding environment in the Ge lattice we calculated the electron localization function (ELF)[34] which provides a topological spatial map of quantum mechanical effects related to the Pauli exclusion principle.[35] The isosurfaces of the ELF roughly mimic the classical Lewis description of bonding and provide a systematic spatial picture of bonding and nonbonding electron pairs. In particular the ELF ranges in value from 0 to 1, where 1 corresponds to perfect localization. Figure 12 shows a plot of the ELF through the [110] plane of the 64-atom supercell, clearly revealing the ellipsoidal charge pockets characteristic of tetrahedral Ge bonding (gray pockets, representing one electron per bond, localized midway between Ge sites with a medium gray value ~ 0.6). The group-V dopant atoms are situated in the center of each panel and exhibit a higher value of ELF (close to 1) along the bonds to the neighboring Ge atoms. We note that the degree of electron localization along the M−Ge decreases along the sequence P, As, and Sb and that a mild localization accrues on the dopant atom centers along the same sequence. An identical picture emerges if one examines the ELF in the orthogonal $[\bar{1}\bar{1}0]$ plane, indicating that the five valence electrons associated with the dopant atoms are uniformly distributed among the four tetrahedral bonds with a nominal bond valence of 1.25 e. By contrast, an analogous analysis for the molecular $M(Ge_3)_3$ species reveals ELF basins of value ~ 0.65 along the M−Ge bonds, with an ELF distribution representing a lone-pair protruding from the apex of the molecule.

Conclusions

We developed a new family of carbon-free single-source inorganic hydrides, $M(GeH_3)_3$ (M = P, As, Sb), to enable efficient, safe, and routine group V doping of Si−Ge−Sn semiconductor materials. The vibrational behavior of the precursors is interpreted using density functional theory calculations, which accurately reproduce all of the observed spectra. Simulations were then used to elucidate the structure and thermodynamic stability of the molecules. Proof of principle was demonstrated by the growth of essentially strain-free $Ge_{0.97}Sn_{0.03}$(As) films with As concentration ~ 2×10^{19} atoms/cm^3. TEM, SIMS, AFM, RBS, and HRXRD characterizations showed defect-free interfacial morphology, excellent compositional uniformity, very low surface roughness, and exceptional crystallinity. A contactless ellipsometric technique was then used to determine electrical properties of the doped films. Typical values for the resistivity and relaxation time are $\rho_0 = 0.0124\ \Omega$ cm and $\tau = 1.14 \times 10^{-14}$ s, while an effective mass $m^* = 0.094m_e$ (average of the L-valley and the Γ-valley masses) was found to bring ellipsometric and SIMS measurements of the concentration data into agreement. Finally, the trends in the lattice relaxation induced in the Ge-rich materials lattice by dopant atoms was studied using density functional theory simulations. We find that while the first neighbor shell bonding around the substitutional dopant atom follows the trends in the molecular $M(GeH_3)_3$ bonding, all dopants produce a slight net positive lattice strain. From the calculated ground state properties of the Ge, P, As, and Sb solid phases we estimate the substitution (incorporation) energies of P, As, and Sb into Ge to be +0.31, +0.31, and +0.56 eV, respectively. An analysis of the charge density of the doped lattice indicates that electron localization is enhanced in the M−Ge bonds (M = P, As, Sb) compared with Ge−Ge bonds, suggesting that all bonding electrons on the group V dopant contribute to the tetrahedral (over-) bonding in the crystalline setting.

Experimental Section

General Procedures. All manipulations were carried out under inert conditions using standard Schlenk and drybox techniques. Dry,

(30) Kikegawa, T.; Iwasaki, H. *Acta Crystallogr.* **1983**, *B39*, 158−164.
(31) Schiferl, D.; Barrett, C. S. *J. Appl. Crystallogr.* **1969**, *2*, 30−36.
(32) Donohue, J. *The Structures of the Elements*: Wiley-Interscience, New York, 1974.
(33) Young, D. A. *Phase Diagrams of the Elements*; University of California Press: Berkeley, 1991; pp 278−281.
(34) Becke, A. D.; Edgecombe, K. E. *J. Chem. Phys.* **1990**, *92*, 5397.
(35) Silvi, B.; Savin, A. *Nature* **1994**, *371*, 683.

air-free solvents were distilled from either anhydrous $CaCl_2$ or sodium benzophenone ketyl prior to use. All NMR spectra were collected either on a Varian INOVA 400 spectrometer operating at 400 MHz or a Gemini 300 spectrometer. Samples were dissolved in $CDCl_3$, and all nuclei were referenced either directly or indirectly to the proton signal of TMS or the residual solvent peak as indicated. IR spectra were recorded using a 10 cm gas cell with KBr windows. The starting materials GeH_3Br and $(SiMe_3)_3E$ (E = P, As, Sb) were prepared according to literature procedures, and their purity was checked by NMR spectroscopy.[10a−d] Semiconductor grade GeH_4 was obtained from Voltaix Corp.

Synthesis of $(GeH_3)_3P$. A 100 mL round-bottom flask, containing a Teflon-coated stir bar, was charged with 0.980 g (3.9 mmol) of $(Me_3Si)_3P$[10b] and was subsequently cooled to −196 °C and degassed. Freshly prepared $BrGeH_3$, 2.34 g (15.1 mmol; 280 L Torr), was condensed into the flask and slowly warmed to 0 °C. The mixture was stirred at 0 °C for 17 h, upon which a very small amount of a light yellow-colored precipitate had formed. The volatiles were fractionally distilled through −22 °C, −45 °C, and −196 °C traps without pumping under static pressure. The contents of each trap were analyzed *via* gas-phase FTIR spectroscopy which revealed the presence of $(GeH_3)_3P$ (−22 °C trap), trace Br_2GeH_2 (−45 °C trap), Me_3SiBr, residual GeH_4, and H_3GeBr (−196 °C trap) by comparing the spectra to those of authentic samples. Trigermylphosphine was redistilled through a −25 °C trap under dynamic vacuum resulting in a pure colorless liquid product (0.720 g, yield = 72%). Trigermylphosphine decomposes slowly over time at room temperature to give germane and an involatile substance. Its vapor pressure is ∼5 Torr at 23 °C and 1 Torr at 0 °C. FTIR (gas, cm^{-1}): 2080 (s), 875 (w), 839 (w), 798 (vs), 563 (vw), 515 (vw). ^1H NMR ($CDCl_3$): δ 3.84 (d, Ge-H).

Synthesis of $(GeH_3)_3As$. A 100 mL, round-bottom flask, containing a Teflon coated stir bar, was charged with 1.80 g (6.1 mmol) of $(Me_3Si)_3As$, and the flask was cooled to −196 °C and degassed. Freshly prepared $BrGeH_3$, 3.42 g (22.0 mmol; 408 L Torr) was condensed into the flask and slowly warmed to 0 °C. The mixture was stirred at 0 °C for 17 h, upon which a very small amount of an amber-colored precipitate formed. The volatiles were fractionally distilled through a −15 °C, −45 °C, and −196 °C trap under dynamic vacuum. The contents of each trap were analyzed *via* gas-phase FTIR spectroscopy which revealed the presence of $(GeH_3)_3As$ (−15 °C trap), trace Br_2GeH_2 (−45 °C trap), Me_3SiBr, residual GeH_4, and H_3GeBr (−196 °C trap). Trigermylarsine was redistilled through a −20 °C trap under dynamic vacuum resulting in a pure colorless liquid product (1.29 g, yield = 70%). Trigermylarsine decomposes slowly at room temperature to give germane and an involatile substance. Its vapor pressure is ∼1 Torr at 23 °C. FTIR (gas, cm^{-1}): 2077 (s), 873 (w), 829 (w), 785 (vs), 528 (vw), 489 (vw). ^1H NMR ($CDCl_3$): δ 3.896 (s, Ge-H).

Synthesis of $(GeH_3)_3Sb$. A 100 mL, round-bottom flask, containing a Teflon coated stir bar, was charged with 0.978 g (2.9 mmol) of $(Me_3Si)_3Sb$, and the flask was subsequently cooled to −196 °C and degassed. Freshly prepared $BrGeH_3$, 1.54 g (9.9 mmol; 184 L Torr), was condensed into the flask and slowly warmed to −8 °C. The mixture was stirred at −8 °C for 13 h, upon which a very small amount of an amber-colored precipitate had formed. The volatiles were fractionally distilled through −25 °C, −45 °C, and −196 °C traps under dynamic vacuum. FTIR revealed the $(GeH_3)_3Sb$ in the −25 °C trap and trace Br_2GeH_2 in the −45 °C trap, as well as Me_3SiBr, residual GeH_4, and H_3GeBr in the −196 °C trap. Trigermylstibine was redistilled through a −25 °C trap under dynamic vacuum resulting in a pure colorless liquid product (0.70 g, yield = 70%). Trigermylstibine decomposes slowly at room temperature to give germane and an involatile substance. Its vapor pressure is about 0.50 Torr at 23 °C. FTIR (gas, cm^{-1}): 2060 (s), 838 (w), 798 (w), 768 (vs). ^1H NMR ($CDCl_3$): δ 3.529 (d, Ge−H).

Acknowledgment. The work was supported by NSF (DMR 0221993 and 0526604) and Intel Corporation. We thank Dr. M. Bauer for the initial studies related to this work.

CM061696J